The lower energy diffraction and scattering side-bounce beamline for materials science at the Canadian Light Source

Adam F. G. Leontowich,[a] Ariel Gomez,[a] Beatriz Diaz Moreno,[a] David Muir,[a] Denis Spasyuk,[a] Graham King,[a] Joel W. Reid,[a] Chang-Yong Kim[a] and Stefan Kycia[b]*

[a]Canadian Light Source, 44 Innovation Boulevard, Saskatoon, Saskatchewan, Canada S7N 2V3, and [b]University of Guelph, 50 Stone Road E, Guelph, Ontario, Canada. *Correspondence e-mail: skycia@uoguelph.ca

A new diffraction beamline for materials science has been built at the Canadian Light Source synchrotron. The X-ray source is an in-vacuum wiggler with a 2.5 T peak magnetic field at 5.2 mm gap. The optical configuration includes a toroidal mirror, a single side-bounce Bragg monochromator, and a cylindrical mirror, producing a sub-150 µm vertical × 500 µm horizontal focused beam with a photon energy range of 7–22 keV and a flux of 10^{12} photons per second at the sample position. Three endstations are currently open to general users, and the techniques available include high-resolution powder diffraction, small molecule crystallography, X-ray reflectivity, in situ rapid thermal annealing, and SAXS/WAXS. The beamline design parameters, calculated and measured performance, and initial experimental results are presented to demonstrate the capabilities for materials science.

1. Introduction

The Lower Energy (LE) beamline is one of three beamlines that form the Brockhouse X-ray Diffraction and Scattering (BXDS) sector at the Canadian Light Source (CLS) synchrotron. These hard X-ray beamlines were purpose-built for diffraction and scattering experiments, primarily for the materials science communities in Canada and abroad. The techniques currently available to users of this sector include high-resolution powder diffraction, pair distribution function (PDF), reflectometry and grazing incidence diffraction, reciprocal space mapping, small molecule crystallography, in situ and extreme conditions experiments, single-crystal/magnetic/anomalous diffraction, and small/wide angle X-ray scattering (SAXS/WAXS). The sector is intended to facilitate both fundamental and industrial research, as demonstrated by very productive beamlines around the world with a similar scientific scope (Wang et al., 2008; Thompson et al., 2009; Hexemer et al., 2010; Strempfer et al., 2013; Lausi et al., 2015).

The LE beamline is the focus of this article. However, major aspects of its design, including the source and monochromator, were highly influenced by its close proximity to the other two BXDS beamlines. We will briefly describe the overall design of the sector in this context. The initial motivation and science case for the sector called for at least one source of intense, very high-energy X-rays. For example, operando measurements of batteries and high-pressure experiments in diamond anvil cells require high energies of $\geq$30 keV to penetrate the sealed sample environments. For PDF measurements, the minimum resolution is dependent on the maximum scattering vector, Q_{max}, which is proportional to the incident photon

50 mm
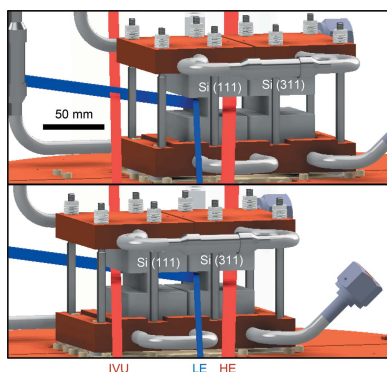
© 2021 International Union of Crystallography

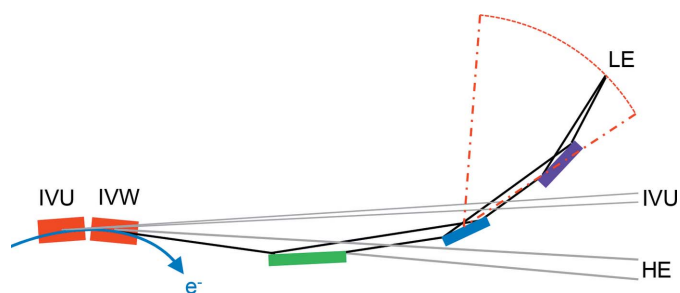https://doi.org/10.1107/S1600577521002496 **961**

Figure 1
Not-to-scale schematic of the LE beamline and its relationship with the other two hard X-ray beamlines of the Brockhouse sector. The major optical elements are a toroidal mirror (green), a planar Si crystal (blue), and a cylindrical mirror (purple).

energy and the largest scattering angle collected by the detector. Considering some practical limitations on detector geometries, 40–80 keV is ideal for high-resolution PDF measurements. These high-energy experiments, in particular, cannot be sourced by an undulator at the 2.9 GeV CLS and called for a high magnetic field wiggler.

The completed BXDS sector has two insertion devices, sharing straight Section 4 of the CLS storage ring. A high-field in-vacuum wiggler (IVW, 04ID-2) occupies the downstream half. The IVW is the source for two beamlines. A Higher Energy (HE) beamline (20–100 keV) accepts the on-axis central portion of the IVW emission. A second IVW beamline, the LE beamline (7–22 keV), was created using a side-bounce mirror. This mirror intercepts the inboard off-axis portion of the IVW beam and deflects it outboard. An in-vacuum undulator (IVU, 04ID-1), canted at 4.0 mrad relative to the IVW, occupies the upstream half of the straight and is the source for one beamline (5–24 keV). The overall layout of three independent beamlines from two insertion devices is depicted in Fig. 1.

Here we present the BXDS LE beamline, including the unique IVW and optical design solutions. The BXDS HE (Gomez et al., 2018) and IVU (Diaz et al., 2014) beamlines have been reported previously elsewhere. The calculated performance is presented and compared to results collected during the beamline commissioning period. We also briefly describe the capabilities of the three endstations of this beamline, which have recently entered general user operation.

2. In-vacuum wiggler source

A magnetic field of >2 T is necessary to produce intense X-rays of >40 keV at a medium energy synchrotron like the CLS (Marcouille et al., 2013). A quick calculation of the deflection parameter K of a >2 T insertion device reveals that K is always ≫1 for practical magnetic periods of >10 mm (Kim, 1986). Therefore, the source which best meets the requirements for the highest energy techniques at the BXDS sector is a wiggler. Wigglers also offer a broad smooth spectrum at a fixed gap, which is ideal for running multiple independent beamlines from one source.

Although very high fields have been achieved in superconducting wigglers, a permanent magnet IVW was chosen for BXDS. IVWs are relatively uncommon but have proved to be successful solutions elsewhere (Maréchal et al., 2001; Shi et al., 2004; Marcouille et al., 2013, 2019). A superconducting design could have offered approximately three and ten times higher flux for the LE and HE beamlines, respectively. However, these devices come with additional infrastructure requirements, continuous maintenance, and downtime due to their complex cooling systems. This can be a significant draw on resources over the lifetime of the facility, in addition to the higher purchase price. Other benefits and drawbacks of the IVW design have been reported elsewhere (Maréchal et al., 2001; Shi et al., 2004; Marcouille et al., 2013, 2019).

The IVW was built by the Shanghai Synchrotron Radiation Facility (SSRF). It has a hybrid magnetic structure, with Sm_2Co_{13} (R32HS) permanent magnets and V permendur (vacoflux 50) poles, which were shaped to maximize the peak field. The magnet arrays have 16 periods of 80.0 mm length, plus the endsections. The large magnetic forces involved are counteracted by compensating springs. A peak magnetic field of 2.5 T was measured between the poles at the design minimum gap of 5.2 mm, which translates to a K value of 18.7 if the magnetic field is treated as purely sinusoidal. However, this approximation is not valid for high-field and long-period insertion devices, and higher harmonics appear (Maréchal et al., 2001). Taking this into consideration, we calculated an effective field of 1.9 T at the design minimum gap of 5.2 mm, and an effective K value, K_e, of 14.2, yielding a critical energy of 10.6 keV and a maximum power of 6.15 kW at the CLS maximum ring current of 250 mA. This design assured high flux at 60 keV, while avoiding contamination to the adjacent IVU beam (K_e/γ = 2.5 mrad, where γ is the relativistic Lorentz factor). The IVW X-ray source size, Σ, and divergence, Σ', were calculated to be (H × V) 663 μm × 43 μm and 1.207 mrad × 0.105 mrad, respectively. These calculations were performed using SPECTRA (Version 10.2; Tanaka & Kitamura, 2001), with current storage ring parameters.

Commissioning of the IVW in the storage ring began in January 2017 and exposed a problem in achieving the design minimum gap. Extensive modeling and investigation revealed issues with a Cu–Ni foil covering the magnet arrays. The foil serves to manage the wakefield and heat load from the stored electron beam, and its configuration becomes even more critical for the implementation of two canted insertion devices (Shi et al., 2004; Huang et al., 2015). A redesign of the foil system was initiated, including a new foil of higher quality, an improved foil tensioning system and new flex tapers. Upon replacing these components, 5.2 mm gap at maximum ring current was achieved in May 2019 after a one week long conditioning period. Further details of these efforts will be presented as a separate publication.

There are three sequential water-cooled Cu fixed masks in the front end of the sector. The third and final mask has one opening for the IVW and another for the IVU, and defines the maximum possible acceptance of both sources. This mask is 12.079 m from the center of the IVW, and the rectangular
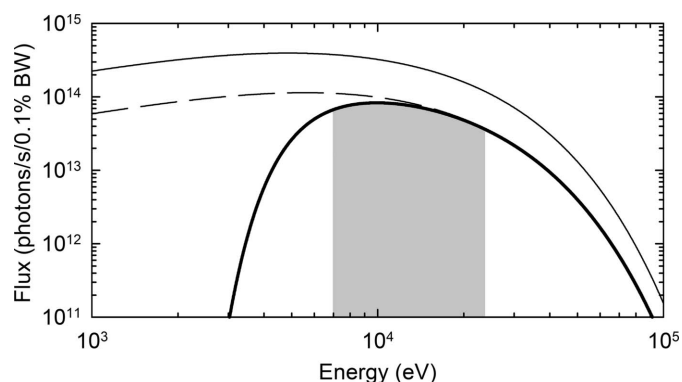
Figure 2
Calculated IVW flux for maximum operating conditions of 5.2 mm gap, 1.9 T effective field, and 250 mA ring current. The energy range of the LE beamline is shaded. (Thin solid line) All IVW flux through the final mask. (Dashed line) Flux available for the LE beamline, considering the offset of the final mask and the beamline acceptance of 0.27 mrad H × 0.40 mrad V. (Thick solid line) Flux available for the LE beamline, considering the offset of the final mask, the beamline acceptance, and the two fixed graphite filters.

Table 1
Beamline components, distances and calculated power loads for maximum operating conditions of 5.2 mm gap, 1.9 T effective field, and 250 mA ring current. The power load calculations were made using *SPECTRA*.

Number	Component	Distance from IVW center to component center (m)	Absorbed power (W)	Through power (W)
N/A	IVW	N/A	N/A	6150
1	Fixed mask 3 (final mask)	12.079	4910	1240
2	APG filter, 150 µm	13.398	290	950
2	APG filter, 200 µm	13.480	104	846
2	APG filter, 1000 µm*	13.655	212	634
2	Vertical slits, 5.5 mm	13.767	44	802
3	Toroidal mirror	15.243	90	173 to LE 539 to HE
4	Diamond screen*	18.260	40	N/A
4	Fixed mask	18.748	N/A	173
4	Antiscatter slits	18.969	<1	173
5	Monochromator crystal	19.840	~173	<1
5	Be window	20.440	<1	<1
6	Cylindrical mirror	23.840	<1	<1
7a	Endstation, IBM	29.090	<1	N/A
7b	Endstation, Bruker	31.090	<1	N/A
7c	Endstation, Huber	29.090	<1	N/A

Note: (*) the optional 1000 µm graphite filter and diamond screen are considered to be out of the beam for the power loads of the components downstream.

aperture for the IVW beam is 10.30 mm H × 5.83 mm V. The IVW emission is centered vertically in this aperture, while horizontally it is positioned 1.63 mm outboard from the center, to maximize the flux of high-energy photons for the HE beamline. The LE beamline centerline is positioned 4.65 mm inboard (0.385 mrad) of the IVW centerline. The flux of the IVW after the final mask was calculated using *SPECTRA* and is presented in Fig. 2.

3. Beamline design

A scale drawing overview of the LE beamline is presented as Fig. 3, and the component distances and power loads are tabulated in Table 1.

The first components after the front end masks are three annealed pyrolytic graphite (APG) plates clamped in water-cooled Cu frames, similar in design to those of Cambie *et al.* (2004). These high-pass filters suppress X-rays of ≤5 keV (Fig. 2), which are not useful for the science scope of this sector, and reduce the heat load on the optics downstream. The first two are fixed, while the third is optional *via* a pneumatic actuator. These are followed by a set of motorized water-cooled vertical slits, which are normally held at a 5.50 mm gap centered on the beam, defining the LE beamline vertical acceptance at 0.40 mrad.

The first optic is a side-bounce toroidal mirror with indirect water cooling. This mirror serves three functions: (i) it reflects an inboard portion of the IVW beam outboard, towards the LE beamline monochromator, separating the IVW emission into two beams (Fig. 1); (ii) it collimates the beam in the horizontal (meridional radius = 8.889 km), in preparation for the monochromator; and (iii) it focuses the beam in the vertical (sagittal radius = 49.59 mm) to the sample position, 13.847 m downstream. The Si substrate has a coating of 5 nm Rh, on top of 35 nm Pt, on top of a Cr binding layer. The coating was optimized for a 3.43 mrad incidence angle and,

with the mirror total length of 1.200 m, results in a horizontal beamline acceptance of 0.27 mrad, or a 4.1 mm horizontal beam size at the mirror. The mirror and cooling assembly rest on a three-point kinematic mount inside a vacuum chamber. The chamber can be manipulated about five degrees of freedom (no translation along the beam axis) using a motorized three jack system.

Downstream of the mirror is a 200 µm-thick diamond screen clamped in a motorized water-cooled Cu frame. The screen is a diagnostic for aligning the toroidal mirror, and is typically retracted out of the beam at all other times. A water-cooled Cu mask follows the screen, and prevents any mis-steered IVW or IVU beams from striking unintended places further downstream. The fixed mask is followed by a set of motorized water-cooled vertical slits, which prevent any stray scattered radiation from the toroidal mirror from entering the monochromator. Each blade is typically set to clip ≤1% of the intensity.

The monochromator is a single side-bounce design, in which a planar Si crystal deflects the LE beam further outboard at a 2θ angle of 14.2–32.8°. This is not a common design choice for a modern materials science beamline. Most beamlines with a comparable science scope use vertically oriented double-bounce designs, such as channel-cut or double-crystal mono-chromators. But the single side-bounce design is critical to enabling three beamlines on one storage ring straight section, and there are operational advantages discussed at the end of this section.

The monochromator includes a choice of two crystals, Si(111) or Si(311). The availability of two crystals provides a trade off between flux and energy resolution, and an increased
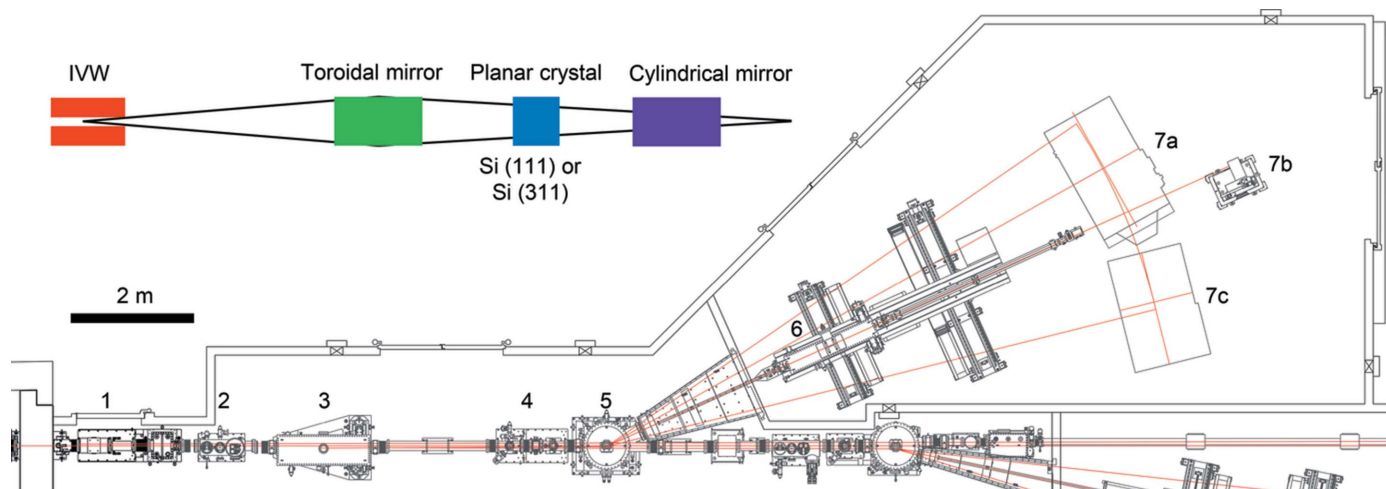
Figure 3
(Top left) Not-to-scale schematic of the LE beamline, side view. (Bottom) A scale drawing of the LE beamline, top view. The drawing depicts the components downstream of the thick storage ring shielding wall at the left. The component numbering is described in Table 1.

energy range. Both crystals are mounted in a liquid nitrogen (LN_2)-cooled carriage providing side cooling, and the carriage is manipulated in vacuum using three vacuum-compatible motorized stages providing rotation (θ), translation (crystal selection and centering), and tilt (pitch from the endstation perspective). The powerful IVU, HE, and LE beams traverse the LE monochromator in close proximity on the same horizontal plane (Fig. 1). This engineering challenge resulted in the unique design of the crystals and the carriage (Fig. 4), which allows the LE monochromator to function while the IVU and HE beams pass through unobstructed. The LE beam exits the monochromator vacuum chamber through a 243 mm × 14 mm × 254 µm Be window. The monochromator and all of the components upstream have a windowless connection to the storage ring, and achieve ultra-high vacuum (UHV) with a base pressure of 10^{-9} Torr with the shutters open under maximum operating conditions.

By Bragg's law, beams of different energies exit the single side-bounce monochromator at different horizontal angles. To take advantage of this, all of the beamline components downstream of the monochromator, including a cylindrical mirror, ion chambers, filters, slits, *etc.*, are mounted on top of a 4 m long translating table in the experimental hutch. The table is aligned with the rotation axis of the monochromator (θ), and has a travel range 2θ = 14.2–32.8°. The final optical component is a side-bounce cylindrical mirror which focuses the beam in the horizontal to the sample location. This second mirror has a 3.158 km meridional radius and a choice of two coating stripes, Cr and Pt, on the Si substrate, for higher harmonic suppression. The design incidence angle is 3.32 mrad, and with a total length of 1.300 m, it accepts a 4.3 mm beam in the horizontal. The mirror rests on a kinematic mount inside a separate vacuum chamber, with 130 µm-thick Be entrance and exit windows, and is maintained at 10^{-10} Torr with the shutters open. The chamber can be manipulated about five degrees of freedom using a motorized three-jack system, identical to that of the toroidal mirror.

The single side-bounce monochromator changes the way we think about energy scanning for the endstations. Comparable beamlines with more common double-bounce monochromators are operated such that the θ angle of the first crystal selects a desired photon energy, and then the second crystal diffracts the beam back to the original direction. This enables energy tuneability at a fixed endstation location. At the LE beamline, we have implemented coordinated motion of the monochromator θ angle with the 4 m translating table carrying the downstream beamline components. This accomplishes the same function from the endstation frame of reference, for
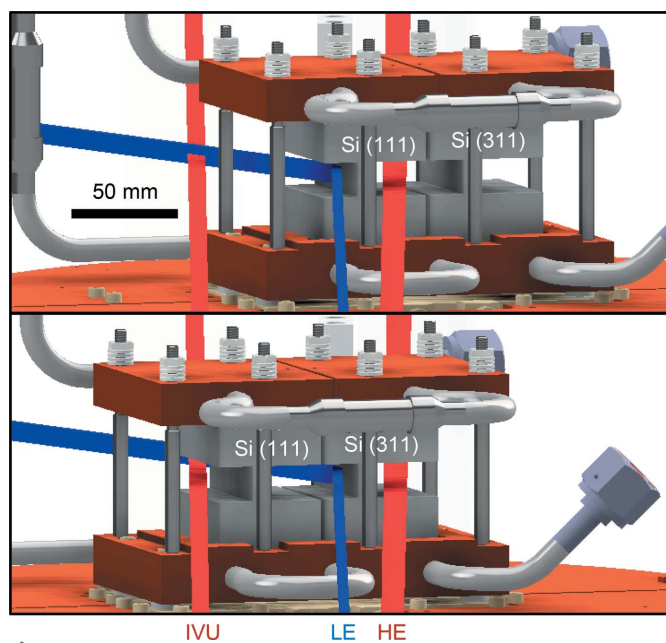

Figure 4
CAD model of the LN_2-cooled crystal carriage of the LE monochromator, upstream view, with all three BXDS beams depicted. The scale bar is for dimensions perpendicular to the beam, and both panels are on the same scale. (Top) Si(111) in position with $\theta = 16°$ and (bottom) Si(311) in position with $\theta = 16°$.

an endstation mounted on the translating table. We have measured the X-ray absorption spectra of metallic reference foils using two ion chambers mounted on the translating table for accurate energy calibration. Endstations could be permanently located on the table in the future. On the other hand, many hard X-ray diffraction and scattering techniques, such as powder diffraction and small molecule crystallography, do not require energy scanning for most applications. Multiple endstations serving multiple communities can be set up along the focal arc of the beamline, and we can quickly change between them. At present, three endstations are positioned on the hutch floor, at fixed energies: the high-resolution powder diffraction endstation ($2\theta = 15°$), the small-molecule crystallography endstation ($2\theta = 24°$), and the *in situ* rapid thermal annealing endstation ($2\theta = 29°$). These will be described in a later section (§5).

4. Beamline performance

Flux, beam size, energy resolution, and divergence were calculated using the *SHADOW3* (Sanchez del Rio *et al.*, 2011) ray-tracing module within *XOP* (Version 2.4; Sanchez del Rio & Dejus, 2011), combined with results from *SPECTRA*. The calculation results presented here were performed for the optimum focus location, 29.09 m downstream of the center of the IVW, and under maximum operating conditions of 5.2 mm minimum gap, 1.9 T effective field, and 250 mA ring current. When measuring actual performance, we used the same design acceptance of 0.27 mrad H × 0.40 mrad V as the calculation, with no additional slits along the optical path.

4.1. Flux at the endstations

The flux calculated along the focal arc of the beamline is presented in Fig. 5. For Si(111), the shape of the curve has a strong dependence on the transmission function of the permanent APG filters at lower energies, while at higher
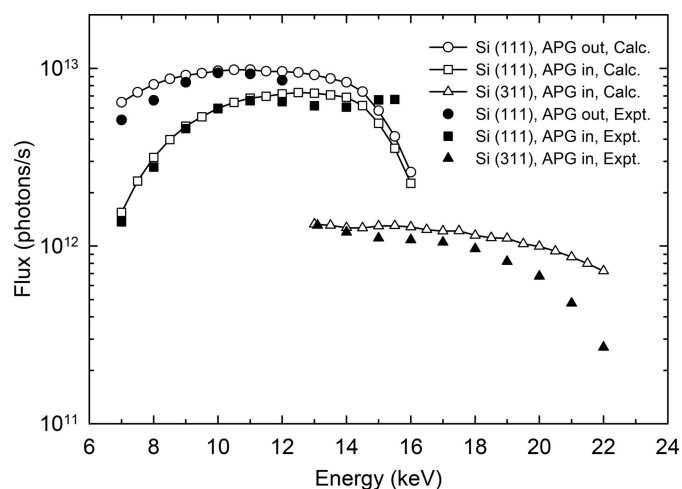
energies, the reflectivity function of the Cr coating on the cylindrical mirror dominates. The Si(311) crystal extends the energy range of the beamline to about 22 keV, above which the flux decreases dramatically, following the reflectivity function of the Rh coating on the toroidal mirror. Removing the optional and pneumatically actuated APG filter from the ray-tracing model offers a boost in flux, although the practical significance is highly energy dependent. A 400% flux increase was predicted at 7 keV, but the benefit drops to 30% by 12 keV. The optics can safely handle the additional power load without this filter. Typically, the optional filter and additional attenuation from a motorized filter wheel in the experimental hutch are required to prevent detector saturation events.

Flux was measured using an ion chamber at the downstream end of the translating table, operating in the plateau voltage region (Sato *et al.*, 1997) under N_2 gas flow. The measurements and trends presented in Fig. 5 display good agreement with the calculated values, except when approaching the high-energy extremes of both monochromator crystals. This is likely due to small differences in the actual angles of incidence of the toroidal and cylindrical mirrors compared to values used in the calculation. Both mirrors operate at very low angles (3.3–3.4 mrad), where a sub-mrad angle change will shift the position of the reflectivity cut-off by several keV. For these measurements, and in user operation, the mirror angles were set to positions that produced the smallest focused beam size at the endstations.

4.2. Focused beam size

The ray-tracing simulations predicted a full width at half maximum (FWHM) horizontal beam size of 409 µm, constant across the beamline energy range. The predicted FWHM vertical beam size was 77 µm at 7 keV, with a gradual decrease occurring over the full energy range to 66 µm by 22 keV. The decrease is a result of the decreasing divergence of the IVW source at higher energies, and the toroidal figure of the first mirror.

The beam size was measured by two methods: knife-edge scans using motorized slits and an ion chamber, and an 'X-ray eye' (a microscope that collects a magnified image of the X-ray-excited optical luminescence from a thin layer of P43 phosphor on glass). The X-ray eye method provided additional confirmation and a qualitative observation of the whole beam at once and any dynamics. All values of beam size presented below are from knife-edge measurements only.

We found that the best horizontal and vertical focus dimensions were achieved at the predicted distance of 5.25 m downstream of the cylindrical mirror. The best horizontal beam size measured was 413 µm (Fig. 6), with an average value of 455 µm at the three current endstation locations using both monochromator crystals. This is in good agreement with the ray-tracing predictions.

For the vertical focus size measurements, we observed a dependence on the monochromator crystal that was not predicted by ray tracing. The best vertical beam size measured with Si(111) was 110 µm (Fig. 6), with an average value of
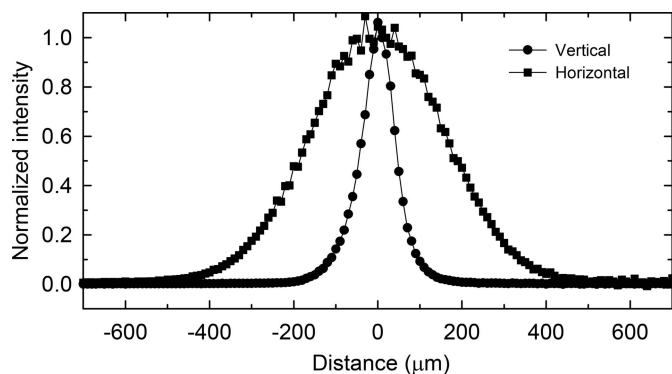
Figure 5
The experimentally determined flux at the endstation locations for maximum operating conditions (solid circles, squares and triangles), overplotted with the predicted values from ray-tracing calculations (open circles, squares and triangles).

Figure 6
The experimentally determined focused beam profile at the endstation location *via* the first derivatives of knife-edge scans.

120 µm at the three endstation locations, whereas the first measurements using the Si(311) crystal approached 500 µm. An investigation of the monochromator revealed that one of the four invar rods which clamps the Si(311) crystal in the LN$_2$-cooled carriage had been partially evaporated, likely during initial radiation testing and conditioning, resulting in an uneven clamping force on the I-beam-shaped crystal (Fig. 4). After repair, the best vertical beam size measured with the Si(311) crystal improved to 129 µm, with an average value of 149 µm at the three endstation locations. In summary, the vertical beam size was found to be about two times the predicted value. Possibly some unintended bending of the monochromator crystals could still be occurring. The calculations do not account for possible crystal slope errors; crystal metrology could not be performed due to scheduling pressures. Other possibilities include the thermal bump on the toroidal mirror and inaccuracies in best estimate values used to model the IVW source (§4.4).

4.3. Energy resolution

The calculated and measured energy bandwidth is presented in Fig. 7. The energy bandwidth of a crystal, ΔE, is
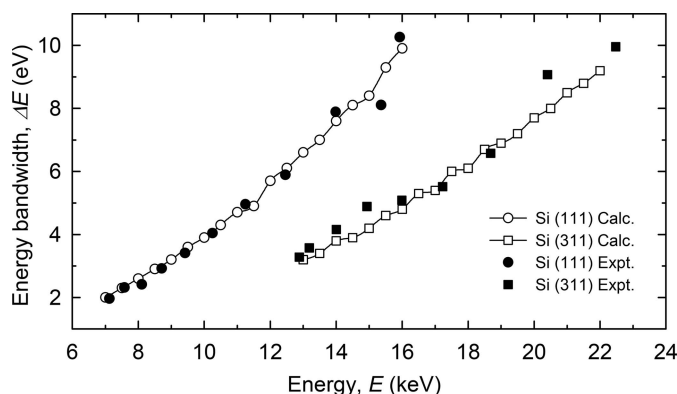

Figure 7
The experimentally determined energy bandwidth after the cylindrical mirror (solid circles and squares), overplotted with the predicted values from ray-tracing calculations (open circles and squares).

$$\Delta E = E \cot\theta \sqrt{\Delta\theta_{cr}^2 + \psi^2} \qquad (1)$$

where E is the energy, θ is the monochromator crystal incidence angle, $\Delta\theta_{cr}$ is the intrinsic crystal Darwin width, and ψ is the divergence of the incident beam in the dispersive plane (Schaefers *et al.*, 2007). The two curves in Fig. 7 correspond to the two crystals available. Si(311) has a narrower $\Delta\theta_{cr}$ at the same E as Si(111), providing a twofold improvement in ΔE for the region where the two crystals overlap. In principle, $\Delta\theta_{cr}$ decreases with increasing E, but this gain is negated by the decrease in θ as E increases. The equation is then dominated by E, causing ΔE to increase linearly as E increases, even for a perfectly collimated incident beam ($\psi = 0$). The deviation from linearity is due to the larger effect of ψ as $\Delta\theta_{cr}$ becomes smaller with increasing E.

The energy bandwidth was experimentally determined by analysing the rocking curves of the (111) and (333) Bragg reflections of a Si(111) single crystal (Batterman *et al.*, 2020). The rocking curve FWHM measurements are convolutions of the Darwin width, the energy bandwidth, and the beam divergence. Energy bandwidth, divergence, and energy can all be extracted from the 2θ positions and FWHM values of the (111) and (333) rocking curves at a chosen energy. A simple instrument was constructed for these measurements, consisting of a two-circle (θ, 2θ) Huber 414 goniometer, a Huber 1003 goniometer head to position the crystal, and a photo-diode detector. The instrument was positioned on the translating table. The Si crystal can be quickly inserted or removed from the beam as required, and the measurement process has been reduced to the execution of a macro. For example, 20 data points covering the full energy range and both crystals can be performed in 8 h.

The experimental results for energy bandwidth are in excellent agreement with the ray-tracing predictions. Expressed as energy resolution, $\Delta E/E$, the measured values for Si(111) ranged from 2.8×10^{-4} at 7.1 keV to 6.4×10^{-4} at 15.9 keV. For Si(311), the measured values ranged from 2.5×10^{-4} at 12.9 keV to 4.5×10^{-4} at 22.5 keV.

4.4. Divergence

Ray-tracing simulations predicted a constant horizontal divergence of 730 µrad across the full energy range of the beamline. The vertical divergence was predicted to be 419 µrad at 7 keV, with a gradual decrease to 241 µrad at 22 keV. These results are presented in Fig. 8. Divergence can also be calculated considering the center of the IVW as a point source and using only the beamline acceptance angles and component distances listed earlier, resulting in values of 784 µrad H × 440 µrad V. The good agreement with more complex ray-tracing simulations shows that the divergence of this beamline is largely due to its geometry. However, the finite source size and divergence, and their dependence on energy, also play a role.

Divergence was determined from measurements of the (111) and (333) reflections of a Si(111) wafer (§4.3). The scattering plane of the instrument was oriented horizontally
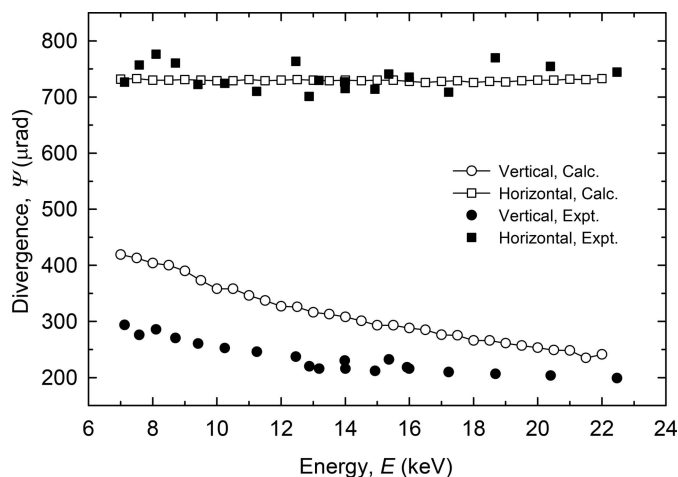
Figure 8
The experimentally determined divergence after the cylindrical mirror (solid circles and squares), overplotted with the predicted values from ray-tracing calculations (open circles and squares).

for the horizontal measurements. Horizontal divergence was found to be 736 µrad, with a standard deviation of 23 µrad over the full energy range, in excellent agreement with the simulation. The measured vertical divergence displayed the predicted decrease over the full energy range, although the values were consistently 70–80% of the predicted values for a given energy.

Some unintended beam clipping may have occurred in the vertical, although the results for beamline flux (§4.1) suggest that the possible extent was minor. The values for the IVW source size and source divergence used in the ray-tracing simulations may be inaccurate; we were unable to measure the complete magnetic field of the IVW due to budget and scheduling pressures, and therefore the simulations rely on an estimated K value and the sinusoidal approximation (§2). A summary of the measured beamline performance is presented in Table 2.

5. Experimental endstations

### 5.1. High-resolution powder diffraction endstation

This endstation is a commercial four-circle diffractometer made by Huber Diffraktionstechnik GmbH & Co. It occupies the inboard side of the hutch, at a default location of $2\theta = 15°$, receiving 15.1 keV photons using the Si(111) monochromator crystal. The endstation is highly flexible, and supports a variety of hard X-ray diffraction techniques with a focus on powder diffraction. A capillary reaction cell (Chupas *et al.*, 2008) is available for measurements under gas flow and temperatures up to 1273 K, ideal for *in situ* catalysis experiments. An ARS DE-202A He cryostat allows studies of phase transformations with temperature control down to 10 K. Multisample stages are available for reflectivity measurements and combinatorial science. A linear Mythen detector (Bergamaschi *et al.*, 2010) with 50 µm pixels, a maximum count rate of 1 MHz per pixel, and a 1 ms minimum read-out time allows the collection of

Table 2
Summary of the measured performance of the LE beamline.

Parameter	Measured values
Flux @ 250 mA, minimum gap	10^{12} photons per second with Si(111), 10^{11} photons per second with Si(311)
Beam size, FWHM	Sub-150 µm V × 500 µm H
Energy resolution, $\Delta E/E$	2.5–6.4×10^{-4}
Divergence	300–200 µrad V × 740 µrad H

high-resolution powder diffractograms and dynamic processes. The powder diffraction resolution achieved (Fig. 9) matches results from other third-generation synchrotron facilities which use this same increasingly common detector (Bergamaschi *et al.*, 2010; Kawaguchi *et al.*, 2017). A crystal analyzer stage, supporting one crystal and one scintillation point detector (C30NA50B, FMB Oxford), is available for experiments requiring even higher resolution. We are currently procuring a sample exchange robot and additional Mythen detectors to increase throughput for powder diffraction. A Rayonix MX300 CCD detector, an evacuated 2.2 m-long flight tube, and active beamstops are available for SAXS/WAXS and grazing incidence experiments. While the beamline motors are controlled with *EPICS*, each endstation has
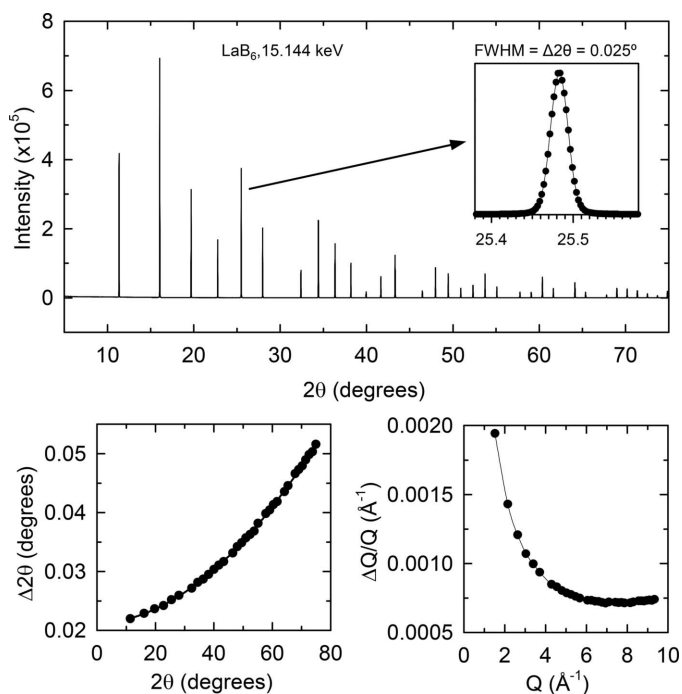
Figure 9
(Top) The powder diffraction pattern of LaB_6 (NIST SRM 660b) in a spinning 0.3 mm inner-diameter Kapton capillary, at 300 K. The pattern was collected at 15.144 keV ($\lambda = 0.81870$ Å), using the Mythen detector at 1189 mm from the sample, with $1°$ steps and 5 s per step. The total measurement time was 10 min. Rietveld refinement was performed using the program *GSAS-II* (Toby & Von Dreele, 2013), and the refinement reached a weighted profile R factor (wR) of 4.7% and a goodness-of-fit (GOF) of 3.7. (Bottom) The instrument resolution function derived from the powder pattern presented (bottom left) as the FWHM of each peak as a function of 2θ, and (bottom right) in momentum transfer Q.

its own control software. This endstation is controlled using *SPEC* Certified Scientific Software (Swislow, 1998).

5.2. Small molecule crystallography endstation

This endstation is a commercial SMART APEX II instrument from Bruker AXS GmbH, and it occupies the middle of the hutch at $2\theta = 24°$, providing fixed energies of 9.5 keV using Si(111) or 18.2 keV using Si(311). The endstation is streamlined for efficient structure determination measurements. It has a three-circle (fixed χ) D8 goniometer with the 2θ rotation axis oriented horizontally. A dovetail track upstream of the sample holds the fast shutter, collimator (50, 200, 300, or 500 μm aperture), and beam stop. An APEX II CCD detector, with 15 μm × 15 μm pixels and a maximum count rate of 2^{16} Hz per pixel, is fixed to the 2θ arm with motorized distance adjustment between 40 and 250 mm. An Oxford 800 series Cryostream provides sample temperature control from 80 to 500 K. *APEX3* software from Bruker is used to control the endstation, acquire the data, and perform the data analysis. It has been used to successfully measure and solve the structure of the Shvo catalyst (Gusev & Spasyuk, 2018), a π-extended squaraine dye molecule (Payne & Welch, 2017), and the thaumatin protein.

5.3. *In situ* rapid thermal annealing endstation

This bespoke endstation was built by a collaboration between Brookhaven National Laboratory and the IBM T. J. Watson Research Center. It is highly optimized for investigating the structural transformations of thin films and multilayers during rapid thermal treatments *in situ*. The cylindrical sample chamber has Be entrance and exit windows, as well as roughness and four-point resistance probes. Samples can be heated rapidly to 1273 K under an atmosphere of ultra-high-purity gas, such as He or N_2. Diffraction patterns are measured using a custom linear strip detector with 640 pixels of 125 μm × 8 mm, a maximum count rate of 1 MHz per pixel, and a 30 ms minimum read-out time. The endstation is completely automated and optimized for remote access, with a sample exchange robot and pneumatic systems to open, close, and lock the sample chamber. A graphical user interface, designed in *LabVIEW* and communicating with *LabVIEW Real-Time Engine*, controls the experiments. Low-level motor control is accomplished with *EPICS*. The endstation was operational and producing scientific results (Dey *et al.*, 2017; Motamedi *et al.*, 2018) at the IDEAS beamline at the CLS before moving to the LE beamline in August 2020. It now occupies the outboard side of the hutch at a $2\theta = 29°$, resulting in fixed energies of 7.9 keV using Si(111) or 15.1 keV using Si(311).

6. Conclusions

A new materials science beamline covering the photon energy range 7–22 keV has been commissioned at the Canadian Light Source. The beamline is dedicated to hard X-ray diffraction and scattering techniques. The intense in-vacuum wiggler

beam is focused to a sub-150 μm V × 500 μm H spot at one of three endstations, with a competitive flux of 10^{12} photons per second on the sample. The beamline is able to operate independently of a second beamline sharing the same wiggler source, owing to a white-beam toroidal mirror deflecting part of the beam outboard. The beamline is fully operational, with all three endstations in general user operation as of January 2021. Detailed up-to-date information for our users can be found on our website at https://brockhouse.lightsource.ca.

References

Batterman, B. W., Shastri, S. D. & Richter, D. E. (2020). *Energy Resolution and Angular Divergence Measurement for Monochromatic Synchrotron Radiation.* CHESS Technical Memorandum (unpublished). Cornell High Energy Synchrotron Source, Ithaca, New York, USA. https://www.chess.cornell.edu/users/calculators/x-ray-calculations-energy-analyzer.

Bergamaschi, A., Cervellino, A., Dinapoli, R., Gozzo, F., Henrich, B., Johnson, I., Kraft, P., Mozzanica, A., Schmitt, B. & Shi, X. (2010). *J. Synchrotron Rad.* **17**, 653–668.

Cambie, D., Cork, C., Duarte, R., Hopkins, C., Lim, A., Lobodovski, A., MacDowell, A., Marks, S., Padmore, H., Pepper, J. & Petermann, K. (2004). *Proceedings of the Third International Workshop on Mechanical Engineering Design of Synchrotron Radiation Equipment and Instrumentation (MEDSI2004)*, 24–27 May 2004, Grenoble, France. MEDSI-Proc-04-04.

Chupas, P. J., Chapman, K. W., Kurtz, C., Hanson, J. C., Lee, P. L. & Grey, C. P. (2008). *J. Appl. Cryst.* **41**, 822–824.

Dey, S., Yu, K.-H., Consiglio, S., Tapily, K., Hakamata, T., Wajda, C. S., Leusink, G. J., Jordan-Sweet, J., Lavoie, C., Muir, D., Moreno, B. & Diebold, A. C. (2017). *J. Vac. Sci. Technol. A*, **35**, 03E109.

Diaz, B., Gomez, A., Meyer, B., Duffy, A., Hallin, E. & Kycia, S. (2014). *Rev. Sci. Instrum.* **85**, 085104.

Gomez, A., Dina, G. & Kycia, S. (2018). *Rev. Sci. Instrum.* **89**, 063301.

Gusev, D. G. & Spasyuk, D. M. (2018). *ACS Catal.* **8**, 6851–6861.

Hexemer, A., Bras, W., Glossinger, J., Schaible, E., Gann, E., Kirian, R., MacDowell, A., Church, M., Rude, B. & Padmore, H. (2010). *J. Phys. Conf. Ser.* **247**, 012007.

Huang, J.-C., Kitamura, H., Chang, C.-H., Chang, C.-H. & Hwang, C.-S. (2015). *Nucl. Instrum. Methods Phys. Res. A*, **775**, 162–167.

Kawaguchi, S., Takemoto, M., Osaka, K., Nishibori, E., Moriyoshi, C., Kubota, Y., Kuroiwa, Y. & Sugimoto, K. (2017). *Rev. Sci. Instrum.* **88**, 085111.

Kim, K.-J. (1986). *Nucl. Instrum. Methods Phys. Res. A*, **246**, 67–70.

Lausi, A., Polentarutti, M., Onesti, S., Plaisier, J. R., Busetto, E., Bais, G., Barba, L., Cassetta, A., Campi, G., Lamba, D., Pifferi, A., Mande, S. C., Sarma, D. D., Sharma, S. M. & Paolucci, G. (2015). *Eur. Phys. J. Plus*, **130**, 43.

Marcouille, O., Bechu, N., Berteaud, P., Brunelle, P., Chapuis, L., Herbeaux, C., Lestrade, A., Marlats, J.-L., Mary, A., Massal, M., Nadji, A., Tavakoli, K., Valleau, M., Veteran, J. & Couprie, M.-E. (2013). *Phys. Rev. ST Accel. Beams*, **16**, 050702.

Marcouille, O., Marteau, F., Tripathi, S., Thiel, A., Tarawneh, H., Tavakoli, K., Marlats, J. L., Mary, A., Valleau, M., Vétéran, J., Chapuis, L., Berteaud, P., Ajjouri, T. E., Brunelle, P., Herbeaux, C., Bechu, N., Lestrade, A., Itie, J.-P., Nadji, A., Guignot, N. & Couprie, M.-E. (2019). *AIP Conf. Proc.* **2054**, 030027.

Maréchal, X.-M., Bizen, T., Hara, T., Seike, T., Tanaka, T. & Kitamura, H. (2001). *Nucl. Instrum. Methods Phys. Res. A*, **467–468**, 138–140.

Motamedi, P., Bosnick, K., Cadien, K. & Hogan, J. D. (2018). *Adv. Mater. Interfaces*, **5**, 1800957.

Payne, A.-J. & Welch, G. C. (2017). *Org. Biomol. Chem.* **15**, 3310–3319.

Sanchez del Rio, M., Canestrari, N., Jiang, F. & Cerrina, F. (2011). *J. Synchrotron Rad.* **18**, 708–716.

Sanchez del Rio, M. & Dejus, R. J. (2011). *Proc. SPIE*, **8141**, 814115.

Sato, K., Toyokawa, H., Kohmura, Y., Ishikawa, T. & Suzuki, M. (1997). *SPring-8 Annual Report*, pp. 225–227. SPring-8, Hyogo, Japan.

Schaefers, F., Mertin, M. & Gorgoi, M. (2007). *Rev. Sci. Instrum.* **78**, 123102.

Shi, C., Jing, Y., Li, D., Peng, Q., Pan, H. B. & Sheng, S. G. (2004). *Proceedings of the 3rd Asia Particle Accelerator Conference (APAC2004)*, 22–26 March 2004, Gyeongju, Korea, pp. 353–355. TUP14004.

Strempfer, J., Francoual, S., Reuther, D., Shukla, D. K., Skaugen, A., Schulte-Schrepping, H., Kracht, T. & Franz, H. (2013). *J. Synchrotron Rad.* **20**, 541–549.

Swislow, G. (1998). *Certified Scientific Software*, http://www.certif.com.

Tanaka, T. & Kitamura, H. (2001). *J. Synchrotron Rad.* **8**, 1221–1228.

Thompson, S. P., Parker, J. E., Potter, J., Hill, T. P., Birt, A., Cobb, T. M., Yuan, F. & Tang, C. C. (2009). *Rev. Sci. Instrum.* **80**, 075107.

Toby, B. H. & Von Dreele, R. B. (2013). *J. Appl. Cryst.* **46**, 544–549.

Wang, J., Toby, B. H., Lee, P. L., Ribaud, L., Antao, S. M., Kurtz, C., Ramanathan, M., Von Dreele, R. B. & Beno, M. A. (2008). *Rev. Sci. Instrum.* **79**, 085105.